DOI: https://doi.org/10.1016/j.oceaneng.2018.03.079

# TITLE: Numerical simulation of a freely vibrating circular cylinder with different natural frequencies

## ABBREVIATED TITLE: Freely vibrating cylinder: simulation

**Dániel Dorogi***

Department of Fluid and Heat Engineering

Institute of Energy Engineering and Chemical Machinery

University of Miskolc

3515 Miskolc-Egyetemváros

Hungary

**László Baranyi**

Department of Fluid and Heat Engineering

Institute of Energy Engineering and Chemical Machinery

University of Miskolc

3515 Miskolc-Egyetemváros

Hungary

*Corresponding author:

Tel.:+36 20 256 8015

Fax: +36 46 565 471

Postal address: 3515 Miskolc-Egyetemváros, Hungary

E-mail: aramdd@uni-miskolc.hu

DOI: https://doi.org/10.1016/j.oceaneng.2018.03.079

## Abstract

This paper deals with the numerical simulation of low-Reynolds-number-flow around a freely vibrating circular cylinder in two-degrees-of-freedom. The governing equations are written in a non-inertial system fixed to the moving cylinder and solved using finite difference method. The natural frequency of the cylinder is chosen to be constant, agreeing with the vortex-shedding frequency for a stationary cylinder at Reynolds number $Re_0$. Systematic computations are carried out for $Re_0$=80, 100, 140 and 180 keeping the mass ratio and structural damping coefficient at $m^*$=10 and $\zeta$=0. The effect of $Re_0$ on the root-mean-square (rms) values of cylinder displacements and drag coefficients is analyzed. Plotting the data set belonging to different $Re_0$ values against $U^*St_0$ makes comparison easier. Local extreme values are found in the rms of streamwise displacement and drag coefficient in the range $U^*St_0$=0.4–0.65. In the vicinity of $U^*St_0$=0.5 the rms of drag approaches zero and the phase angle between the $x$ component of the motion and drag changes abruptly from 0° to 180°. The pressure drag coefficient seems to be responsible for the sudden change. The cylinder follows a distorted figure-eight path in most cases investigated and its orientation changes from clockwise to counterclockwise orbit at around $U^*St_0$=0.5.

DOI: https://doi.org/10.1016/j.oceaneng.2018.03.079

## Highlights:

- A cylinder is investigated in low Re flow at four different natural frequencies.
- Oscillation amplitudes and drag coefficient shift upwards with higher $Re_0$.
- At $U^*St_0 \cong 0.5$ rms of drag approaches zero and cylinder orbit direction switches.
- At $U^*St_0 \cong 0.5$ phase angle between streamwise motion and drag changes by 180º.
- Pressure drag appears to be related to phase angle and orientation switches.

**Keywords:** *circular cylinder; drag coefficient; free vibration; low Reynolds number; natural frequency; phase angle*

DOI: https://doi.org/10.1016/j.oceaneng.2018.03.079

## 1. Introduction

Flow around a circular cylinder is extensively studied due to its practical importance, using both experimental and numerical approaches. The flows are usually classified using Reynolds number based on free stream velocity $U_\infty$, cylinder diameter $d$ and fluid viscosity $\nu$. For stationary cylinders the flow is steady below Re≅47 and twin vortices are attached to the body. At around Re=47 Hopf bifurcation occurs, resulting in an unsteady flow of periodic vortex shedding (Thompson and Le Gal, 2004). Risers, pipes, and underwater structures are good examples of this phenomenon. Periodic vortex shedding from the body can induce high amplitude oscillations, which can cause serious damage to the structure; this phenomenon played an important role in the collapse of Tacoma Narrows Bridge in 1940. Damage to thermometer cases at the Monju fast-breeder nuclear power plant in 1995 leading to a major shutdown of the entire facility was also due to periodic vortex shedding (Nishihara et al., 2005). On the other hand, mechanical energy transferred between the fluid and the moving body can also be beneficial. Possibilities of energy harvesting have been studied e.g. by Bernitsas et al. (2008, 2009) and Mehmood et al. (2013).

Barkley and Henderson (1996), applying linear stability analysis, showed that the flow around a stationary cylinder is two-dimensional (2D) up to Re≅189. Three-dimensional (3D) instability occurs at Re≅189 (Mode-A) and at Re≅259 (Mode B). Thus, the application of a 2D computational code above Re=189 is not justified for a stationary cylinder. For vibrating cylinders, however, experiments by Bearman and Obasaju (1982) and Koide et al. (2002) and numerical simulations by Poncet (2002) showed that synchronization (or lock-in) between vortex shedding and cylinder motion increases the two-dimensionality of the flow compared to the case of a stationary

DOI: https://doi.org/10.1016/j.oceaneng.2018.03.079

cylinder. The upper limit of the two-dimensionality has not been determined due to the large number of influencing parameters.

For the prediction of aerodynamic forces acting on a freely vibrating cylinder researchers often use a forced or controlled oscillation model. This approach is a simplifying model and is often chosen because no equations need to be solved for the cylinder motion. A large number of papers deal with forced oscillation in one-degree-of freedom (1DoF) cylinder motion, where the cylinder is typically restricted to move only in transverse direction (e.g. Williamson and Roshko, 1988; Lu and Dalton, 1996; Meneghini and Bearman, 1997; Kaiktsis et al., 2007; Baranyi and Daróczy, 2013; Tang et al., 2016) or in streamwise direction (e.g. Okajima et al., 2004; Al-Mdallal et al., 2007; Mureithi et al., 2010). There are relatively few papers dealing with two-degree-of-freedom (2DoF) forced motion (e.g. Jeon and Gharib, 2001; Stansby and Rainey, 2001; Baranyi, 2008; Peppa et al., 2016).

Another approach to the investigation of vortex-induced vibrations (VIV) involves an elastically supported cylinder model, where cylinder displacement is caused by lift and drag forces acting on the body. A large number of studies have dealt with this model, including Bishop and Hassan (1964), Bearman (1984, 2011), Sarpkaya (1995, 2004), Jauvtis and Williamson (2004), Williamson and Govardhan (2004), Blevins (1990), Moe and Wu (1990), and Nakamura et al. (2013). Cylinder response is highly influenced by free stream velocity $U_\infty$, natural frequency of the body $f_N$, structural damping $b$, and the mass of the body $m$.

Vibrations due to vortex shedding are often modeled with 1DoF transverse-only motion. Khalak and Williamson (1999) investigated the VIV of a transversely oscillating cylinder and showed that the mass-damping parameter $m^*\zeta$ strongly

DOI: https://doi.org/10.1016/j.oceaneng.2018.03.079

influences the peak amplitude, where $m^*$ is the mass ratio (the ratio of the mass of the vibrating body and that of the displaced fluid) and $\zeta$ is the structural damping coefficient. It was shown that at low $m^*\zeta$ three branches of cylinder response occur, namely initial, upper and lower branches, where the upper branch is associated with the highest oscillation amplitude. Feng (1968) studied high mass-damping cases where only two branches (an initial branch with low cylinder displacements and lower branch with high vibration amplitudes) are observed. Brika and Laneville (1993) and Govardhan and Williamson (2000) distinguished between the different branches based on their vortex-shedding modes. The initial branch is associated with 2S mode (two single vortices are shed in each motion cycle) while 2P mode (two vortex pairs shed in each motion cycle) belongs to the lower and upper branches. Brika and Laneville (1993) found that the transition between upper and lower branches is hysteretic and the flow is quite sensitive to incremental changes in the reduced velocity.

Klamo et al. (2006) investigated how the system transitions between two-branch and three-branch responses. In their study Reynolds number and the structural damping were varied. It was concluded that $m^*\zeta$ alone is insufficient to predict the type of response; Reynolds number is also an important influencing parameter. For small damping and high Re cases a three-branch response was observed, while a two-branch response was found for high damping and low Re cases.

Naturally, structures are not restricted to move only in one direction; in most cases two-degree of freedom (2DoF) oscillations are found. Jauvtis and Williamson (2004), using an elastically supported cylinder, kept the natural frequencies identical in two directions ($f_{Nx} = f_{Ny} = f_N$) and investigated a wide mass ratio range ($m^* < 25$) using an experimental approach. It was found that at high $m^*$ cases ($m^*$=6–25) in-line

DOI: https://doi.org/10.1016/j.oceaneng.2018.03.079

oscillation has only a tiny effect on transverse vibration, which was also found by Zhou et al. (1999) at low Reynolds numbers using numerical techniques. Jauvtis and Williamson (2004) found that a three-branch response occurs, as in 1DoF cylinder oscillation. Upon decreasing the mass ratio below $m^*$=6 dramatic changes were observed. The existence of a super-upper branch was reported where the vortex-shedding mode was 2T type – two triple vortices shed in each vibration period.

However, in general, the natural frequencies in streamwise and transverse directions are not identical, $f_{Nx} \neq f_{Ny}$. Sarpkaya (1995) experimentally investigated 2DoF vortex-induced vibrations varying the natural frequency ratio $f_{Nx}/f_{Ny}$ between 1 and 2. These results were compared with 1DoF cylinder oscillation results for $f_{Nx}=f_{Ny}$ and a 19% increase was observed in the transverse oscillation amplitude. In addition, two obvious peaks were identified at $f_{Nx}=2f_{Ny}$. Dahl et al. (2006) showed that by increasing the ratio of streamwise and transverse frequencies in the range of $f_{Nx}/f_{Ny}$=1–1.9, the phase angle between $x$ and $y$ component of the motion decreases and the peak amplitude shifts to higher reduced velocities $U^*=U_\infty/(f_N d)$, where $f_N=f_{Ny}$ is the transverse natural frequency. Sanchis (2009) extended the frequency ratio range, where the natural frequency in transverse direction was greater than in streamwise direction ($f_{Nx}/f_{Ny}$=0.42, 0.87). The amplitude and frequency responses were very similar to those for $f_{Nx}/f_{Ny}$ =1. The only difference was that the transition between upper and lower branch shifted from intermittency to lag. Kang et al. (2016) investigated three different circular cylinders with distinct aspect ratios ($L/D$=6, 10.91 and 24). It was shown that with high aspect ratios ($L/D$=24) different moving trajectories occur – D-shaped, egg-shaped, raindrop-shaped and figure-eight – but with sufficiently low aspect ratios (such as $L/D$=6) only figure-eight (or rather, distorted figure-eight) motion is found.

DOI: https://doi.org/10.1016/j.oceaneng.2018.03.079

Most of the experimental studies are carried out at the medium range of Reynolds numbers ($Re=10^3–10^4$). Numerical studies at this regime are very limited because of the high computational cost; therefore, most computations are carried out for low Re. Govardhan and Williamson (2006) and Klamo et al. (2006) showed that besides the mass ratio and structural damping, Reynolds number also strongly influences the oscillation amplitude and fluid forces. Although Reynolds number and reduced velocity are not completely independent variables, it is convenient to investigate their effect separately. Leontini et al. (2006) investigated numerically the branching behavior of VIV at Re=200 with $m^*=10$ and $\zeta=0.01$ for transverse-only cylinder motion. A two-branch response was shown where the vortex-shedding mode was 2S in all cases investigated. At the reduced velocity range of $U^*=4.7–6.4$ large amplitude oscillation occurs where positive and negative vortices coalesce. Using the notations introduced by Williamson and Roshko (1988), this vortex configuration is referred to as C(2S) mode.

Singh and Mittal (2005) carried out two sets of computations for 2DoF cylinder motion (1) at Re=100 with varying $U^*$ and (2) at $U^*=4.92$ and varying Re. A two-branch cylinder response was identified with the maximum dimensionless transverse oscillation amplitude of $y_{0max}\cong0.6$. In the first set of computations 2S vortex configuration was observed. For high amplitude transverse oscillations, C(2S) mode was presented, similar to the results obtained by Leontini et al. (2006). The transition at the lower and higher end of the flow is hysteretic. (This was also found by Brika and Laneville (1993) at medium Reynolds numbers for transverse-only motion.) In the second case investigated by Singh and Mittal (2005), when the reduced velocity was fixed at $U^*=4.92$ and Reynolds number was varied, 2S mode was observed below Re=300 and P+S mode above Re=300.

DOI: https://doi.org/10.1016/j.oceaneng.2018.03.079

There are a few numerical studies dealing with constant natural frequencies. In this case a linear function exists between Reynolds number and reduced velocity (Re=$KU^*$, where $K=f_N d^2/\nu$). Willden and Graham (2006) carried out a numerical study for Re=20$U^*$ in which the body was restricted to move only in transverse direction. The flow characteristics are investigated for five different mass ratios of $m^*$=1, 2, 5, 10, 50. Primary, secondary and tertiary responses were identified. The primary response occurred around lock-in, which is always associated with vortex-induced vibration. The secondary response is found to occur only for high mass ratios ($m^* > 5$) and in the tertiary response regime an approximately constant oscillation amplitude can be maintained. Bahmani and Akbari (2010) investigated numerically the separate effects of mass ratio and structural damping for Re=17.9$U^*$ considering 1DoF cylinder motion. It was found that increasing $m^*$ or $\zeta$ has almost the same effect: both the oscillation amplitude and the lock-in domain decrease.

In the following numerical studies carried out for 2DoF cylinder motion, the natural frequencies in both streamwise and transverse direction are identical ($f_{Nx}=f_{Ny}=f_N$=const.). Prasanth et al. (2006) carried out two sets of computations: (1) at fixed $U^*$=4.92 with varying Re and (2) with constant natural frequencies where both Reynolds number and reduced velocity was varied using Re=16.6$U^*$. Hysteretic loops were also found at the lower and higher end of lock-in. It was shown that by reducing the blockage ratio $B$ (the ratio of cylinder diameter and the height of the computational domain) to $B$=1%, hysteresis loops disappear. Prasanth and Mittal (2008) investigated additional blockage ratios (using Re=16.6$U^*$) and concluded that as the blockage is reduced, the size of hysteresis loops decreases and hysteresis completely disappears at $B$=2.5%. The phase shift between lift coefficient and transverse cylinder displacement

DOI: https://doi.org/10.1016/j.oceaneng.2018.03.079

jumps abruptly from 0° to 180° at Re=110. Decomposing the total lift into two components of pressure lift and viscous lift, the authors concluded that the jump is caused by the pressure lift, since the viscous lift remains in phase with the cylinder motion in all of the investigated Re cases.

Mittal and Singh (2005) investigated mainly subcritical Reynolds numbers (Re < 47), where Re was varied with the reduced velocity (Re=3.1875$U^*$). They found that self-excited motion occurs as low as Re≅20, which is a steady-state regime for a stationary cylinder. At low mass ratio ($m^*$=4.73) the dimensionless vortex shedding frequency St does not agree with reduced natural frequency, which was observed also by Williamson and Govardhan (2004). However, when increasing the mass ratio to $m^*$=50, St and $F_N$ curves almost overlap. At Re=33, $F_N$ is approximately identical to St and the oscillation amplitude was low compared to the Re=25 case, where $F_N$ > St and the vibration amplitude was high. The reason is that at Re=33 the lift force and transverse displacement are in antiphase, therefore the energy transferred between the moving cylinder and the fluid is low compared to that of the Re=25 case, where lift and transverse displacement are in phase, meaning that the mechanical energy transfer is higher.

The present numerical study deals with low-Reynolds-number flow around a circular cylinder free to vibrate in both streamwise and transverse directions. The mass ratio is fixed at $m^*$=10 and the structural damping coefficient is set to zero. As can be seen from the literature review, only low natural frequency values have been investigated for 1DoF and 2DoF free vibrations (the coefficient between Reynolds number and reduced velocity $K$ is in the range of 3–20 only). Systematic computations are carried out for constant natural frequencies agreeing with the vortex shedding

DOI: https://doi.org/10.1016/j.oceaneng.2018.03.079

frequency for a stationary cylinder at the Reynolds number of $Re_0$. To the best knowledge of the authors, most of the articles investigating the 2DoF cylinder motion are dealing with $Re_0$=100 and systematic computations analyzing the effect of $Re_0$ have not yet been carried out. The aim of this paper is to expand the $Re_0$ (and with this the natural frequency) domain by investigating the flow characteristics at $Re_0$=80, 100, 140 and 180. Cylinder response, aerodynamic force coefficients, cylinder path and phase angle between the *x* component of the motion and the total drag, pressure drag and viscous drag coefficients are investigated in this study.

The outline of the current paper is as follows. In Section 2 the governing equations, the boundary and initial conditions are introduced and the computational methodology are presented. In Section 3, first, the independence studies are detailed and then the results obtained here are compared with those in the literature. Finally, Section 4 shows the new computational results and in Section 5 conclusions are drawn.



## Nomenclature

| | |
|---|---|
| $b$ | damping [kg/s] |
| CCW | counterclockwise orbit on the upper loop of figure-eight |
| $C_D$ | total drag coefficient, $2F_D/(\rho U_\infty^2 d)$ [-] |
| $C_{Dp}$ | pressure drag coefficient [-] |
| $C_{Dv}$ | viscous drag coefficient [-] |
| $C_L$ | total lift coefficient, $2F_L/(\rho U_\infty^2 d)$ [-] |
| $C_{Lp}$ | pressure lift coefficient [-] |
| $C_{Lv}$ | viscous lift coefficient [-] |
| CW | clockwise orbit on the upper loop of figure-eight |

DOI: https://doi.org/10.1016/j.oceaneng.2018.03.079

| | |
|---|---|
| $d$ | cylinder diameter, length scale [m] |
| $D$ | dilation, non-dimensionalized by $U_\infty/d$ |
| DoF | degrees of freedom |
| $F_D$ | drag per unit length of the cylinder [N/m] |
| $F_L$ | lift per unit length of the cylinder [N/m] |
| $F_N$ | reduced natural frequency, $f_N d/U_\infty$ [-] |
| $f^*_{x,y}$ | oscillation frequency in $x$ or $y$ directions, respectively, non-dimensionalized by $d/U_\infty$ |
| $f_N$ | natural frequency of the cylinder [1/s] |
| $f_v$ | natural frequency of the cylinder [1/s] $k$ spring constant [kg/s$^2$] |
| $K$ | coefficient between Reynolds number and reduced velocity for constant natural frequencies, $f_N d^2/v$ [-] |
| $m$ | cylinder mass per unit length [kg/m] |
| $m^*$ | mass ratio, $4m/(d^2\pi\rho)$ [-] |
| $p$ | pressure, non-dimensionalized by $\rho U_\infty^2$ |
| $R$ | radius, non-dimensionalized by $d$ |
| rms | root-mean-square value |
| Re | Reynolds number, $U_\infty d/v$ [-] |
| St | dimensionless vortex shedding frequency, Strouhal number, $fd/U_\infty$ |
| $St_0$ | dimensionless vortex shedding frequency for a stationary cylinder at Reynolds number $Re_0$ |
| $t$ | time, non-dimensionalized by $d/U_\infty$ |
| $u$, $v$ | velocities in $x$ and $y$ directions, non-dimensionalized by $U_\infty$ |
| $U_\infty$ | free stream velocity, velocity scale [m/s] |

DOI: https://doi.org/10.1016/j.oceaneng.2018.03.079

| | |
|---|---|
| $U^*$ | reduced velocity, $U_\infty/(f_N d)$ [-] |
| $x$, $y$ | Cartesian coordinates, non-dimensionalized by $d$ |
| $x_0$, $y_0$ | cylinder displacement in $x$ and $y$ directions, non-dimensionalized by $d$ |
| $\zeta$ | structural damping coefficient, $b/\left(2\sqrt{mk}\right)$ [-] |
| $\Theta$ | phase angle between streamwise and transverse components of the cylinder motion [-] |
| $\nu$ | kinematic viscosity of the fluid [$m^2/s$] |
| $\xi_{max}$, $\eta_{max}$ | number of grid points in peripheral and radial direction, respectively |
| $\rho$ | fluid density [$kg/m^3$] |
| $\Phi$ | phase angle between $x_0$ and $C_D$ [-] |
| $\Phi_p$ | phase angle between $x_0$ and $C_{Dp}$ [-] |
| $\Phi_v$ | phase angle between $x_0$ and $C_{Dv}$ [-] |

Subscripts:

| | |
|---|---|
| $L$ | lift |
| $D$ | drag |
| max | maximum value |
| rms | root-mean-square value |
| $n$ | component in the direction normal to the cylinder surface |
| pot | potential flow |
| 1, 2 | on the cylinder surface, at the outer boundary of the domain |
| 0 | refers to cylinder response ($x_0$, $y_0$) or to a stationary cylinder ($Re_0$, $St_0$) |

## 2. Governing equations and computational method

DOI: https://doi.org/10.1016/j.oceaneng.2018.03.079

In this study two-dimensional constant property incompressible Newtonian fluid flow around a circular cylinder undergoing two-degree-of-freedom (2DoF) free vibration is investigated. The non-dimensional governing equations for this problem are the two components of the Navier-Stokes equations written in a non-inertial system fixed to the moving cylinder, the continuity equation and the pressure Poisson equation. These equations in primitive variables are written as follows:

$$\frac{\partial u}{\partial t}+u\frac{\partial u}{\partial x}+v\frac{\partial u}{\partial y}=-\frac{\partial p}{\partial x}+\frac{1}{\mathrm{Re}}\left(\frac{\partial^2 u}{\partial x^2}+\frac{\partial^2 u}{\partial y^2}\right)-\frac{\mathrm{d}^2 x_0}{\mathrm{d}t^2}, \tag{1}$$

$$\frac{\partial v}{\partial t}+u\frac{\partial v}{\partial x}+v\frac{\partial v}{\partial y}=-\frac{\partial p}{\partial y}+\frac{1}{\mathrm{Re}}\left(\frac{\partial^2 v}{\partial x^2}+\frac{\partial^2 v}{\partial y^2}\right)-\frac{\mathrm{d}^2 y_0}{\mathrm{d}t^2}, \tag{2}$$

$$D=\frac{\partial u}{\partial x}+\frac{\partial v}{\partial y}=0, \tag{3}$$

$$\nabla^2 p=2\left(\frac{\partial u}{\partial x}\frac{\partial v}{\partial y}-\frac{\partial u}{\partial y}\frac{\partial v}{\partial x}\right)-\frac{\partial D}{\partial t}. \tag{4}$$

In these equations $u$, $v$ are the non-dimensional velocity components in $x$ and $y$ directions, $t$ is the non-dimensional time, $p$ is the dimensionless pressure, $\mathrm{d}^2x_0/\mathrm{d}t^2$ and $\mathrm{d}^2y_0/\mathrm{d}t^2$ are the non-dimensional streamwise and transverse acceleration components of the cylinder, and $D$ is the dilation. In Eqs. (1) and (2) $\mathrm{Re}=U_\infty d/\nu$ is the Reynolds number, where $U_\infty$ is the free stream velocity, $d$ is the cylinder diameter, and $\nu$ is the kinematic viscosity of the fluid. Although dilation is zero for incompressible fluids, in Eq. (4) $\partial D/\partial t$ is kept to avoid numerical inaccuracies (Harlow and Welch, 1965).

Figure 1 shows the layout of the computations. The figure shows a circular cylinder with a dimensionless radius $R_1$ and with mass per unit length $m$ placed into a uniform free stream with velocity $U_\infty$. The outer boundary of the physical domain, where the flow is assumed to be undisturbed, is represented by dimensionless radius $R_2$. The rigid cylinder is elastically supported in both streamwise and transverse directions. In this

DOI: https://doi.org/10.1016/j.oceaneng.2018.03.079

study springs are supposed to be linear and the spring constants are chosen to be identical in the two directions ($k_x$=$k_y$=$k$), as are the damping values ($b_x$=$b_y$=$b$).

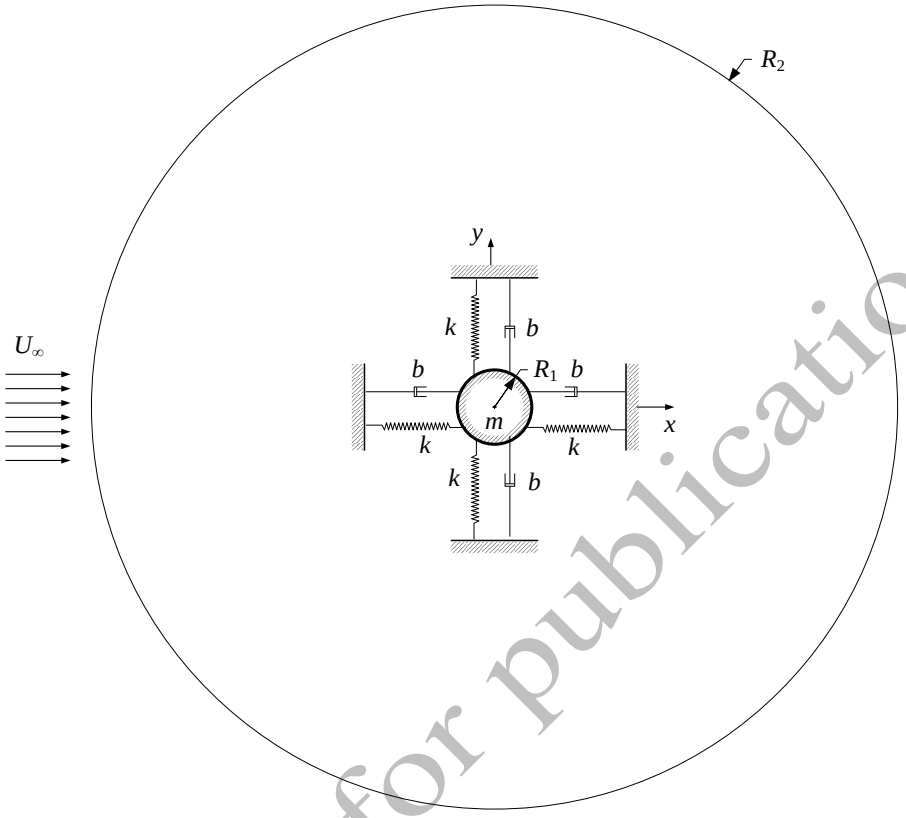


Figure 1. Layout of the elastically supported cylinder



The non-dimensional structural equations that are used to determine the cylinder displacements $x_0$, $y_0$ (Khalak and Williamson, 1999) are written as follows

$$\ddot{x}_0 + \frac{4\pi\zeta}{U^*}\dot{x}_0 + \left(\frac{4\pi}{U^*}\right)^2 x_0 = \frac{2C_D(t)}{\pi m^*}, \tag{5}$$

$$\ddot{y}_0 + \frac{4\pi\zeta}{U^*}\dot{y}_0 + \left(\frac{4\pi}{U^*}\right)^2 y_0 = \frac{2C_L(t)}{\pi m^*}, \tag{6}$$

where dots and double dots mean first and second time derivatives. In these equations $x_0, \dot{x}_0, \ddot{x}_0$ are the dimensionless streamwise displacement, velocity and acceleration of the cylinder, respectively, and $y_0, \dot{y}_0, \ddot{y}_0$ are the same quantities for the transverse direction. In Eqs. (5) and (6) $m^* = 4m/(d^2\pi\rho)$ is the mass ratio, where $\rho$ is the fluid

DOI: https://doi.org/10.1016/j.oceaneng.2018.03.079

density; $U^* = U_\infty/(f_N d)$ is the reduced velocity, where $f_N$ is the natural frequency of the cylinder and $\zeta = b/(2\sqrt{km})$ is the structural damping coefficient. The lift and drag coefficients are defined as

$$C_L = \frac{2F_L}{\rho U_\infty^2 d}, \qquad C_D = \frac{2F_D}{\rho U_\infty^2 d}, \tag{8}$$

where $F_L$ and $F_D$ are the dimensional lift and drag forces per unit length, which are computed from the pressure and shear stress distributions on the cylinder surface. Therefore $C_L$ and $C_D$ can be divided into two parts:

$$C_L = C_{Lp} + C_{Lv}, \qquad C_D = C_{Dp} + C_{Dv}, \tag{9}$$

where subscripts *p* and *v* refer to pressure and viscous parts, respectively. The boundary conditions are written as follows:

Cylinder surface ($R_1$):

$$u = v = 0, \tag{10}$$

$$\frac{\partial p}{\partial n} = \frac{1}{\mathrm{Re}}\nabla^2 v_n - \ddot{x}_{0n} - \ddot{y}_{0n}, \tag{11}$$

Outer surface ($R_2$):

$$u = u_{pot} - \dot{x}_0, \;\; v = v_{pot} - \dot{y}_0, \tag{12}$$

$$\frac{\partial p}{\partial n} = \left(\frac{\partial p}{\partial n}\right)_{pot} \cong 0, \tag{13}$$

where subscript *n* refers to the outer normal of the circular cylinder. On the cylinder surface ($R$=$R_1$) no-slip boundary conditions are applied to the two velocity components *u*, *v* and Neumann-type boundary condition is used for pressure *p*. Potential flow (referred to as subscript 'pot' in Eq. (13)) is assumed in the far field ($R_2$=160$R_1$); it has been shown that this simplification causes only a small distortion in the velocity fields (Baranyi, 2008; Posdziech and Grundman, 2007. Initial conditions for the cylinder displacement and velocity are chosen to be:

$$x_0(t=0) = y_0(t=0) = 0, \qquad \dot{x}_0(t=0) = \dot{y}_0(t=0) = 0. \tag{14}$$

DOI: https://doi.org/10.1016/j.oceaneng.2018.03.079

Potential flow is assumed around the cylinder at $t$=0, hence force coefficients are $C_D$ ($t$=0) = $C_L$ ($t$=0) = 0, which combined with Eqs. (5), (6) and (14) yields zero initial cylinder acceleration $\ddot{x}_0(t=0) = \ddot{y}_0(t=0) = 0$.

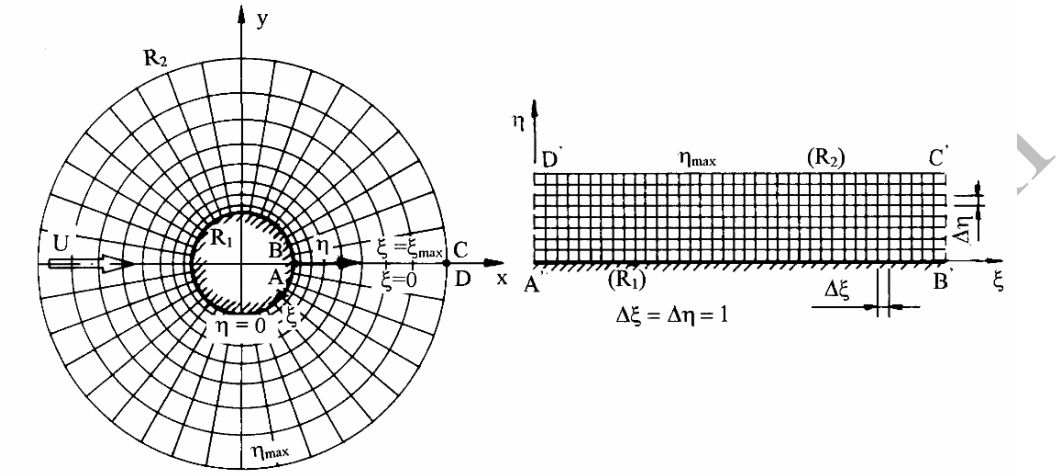


Figure 2. The physical and computational domains

In this study boundary-fitted coordinates are used in order to impose boundary conditions accurately. The physical domain is mapped into a rectangular computational domain (see Fig. 2) applying linear mapping functions (Baranyi, 2008). Due to the properties of the mapping functions, the computational grid on the physical domain is very fine in the vicinity of the cylinder and coarse in the far field, but the grid is equidistant in the computational domain. The transformed governing equations with the transformed boundary and initial conditions are solved using an in-house code based on the finite difference method (Baranyi, 2008). Space derivatives are approximated using fourth-order difference schemes, except for the convective terms where third-order modified upwind difference scheme was applied (Kawamura et al., 1986). The equations of motion and structural equations are integrated explicitly, pressure Poisson

DOI: https://doi.org/10.1016/j.oceaneng.2018.03.079

equation is solved using successive over-relaxation (SOR) method, and the continuity equation is satisfied in each time step.

## 3. Validation procedure

In this section, results of independence studies used to determine the optimal combination of computational parameters are shown. Using this set of parameters, the obtained stationary and elastically supported cylinder results are compared with those available in the literature.

### 3.1 Independence studies

Radius ratio $R_2/R_1$, grid resolution $\xi_{max}\times\eta_{max}$ (grid points in the peripheral and radial direction, respectively), and dimensionless time step $\Delta t$ characterize the computational setup. Independence studies have to be carried out in order to find the optimal combination of the parameters, which is the best compromise between high accuracy and computational cost. During these investigations Reynolds number and reduced velocity are set to be constant values: Re=150 and $U^*$=5.8837. Root-mean-square (rms) values of the dimensionless streamwise, transverse displacements, and lift and drag coefficients are presented.

For investigating the effect of the radius ratio, the number of grid points around the cylinder surface is fixed at $\xi_{max}$=360 and the dimensionless time step is kept at $\Delta t$=0.0005. Three radius ratio values are considered: $R_2/R_1$=120, 160 and 200. In order to make the grid equidistant in the computational domain the number of grid points in the radial direction belonging to the three radius ratio values are chosen to be $\eta_{max}$=274, 291 and 304. The results are given in Table 1. The relative difference between $x_{0rms}$, $y_{0rms}$, $C_{Drms}$ obtained from the results for $R_2/R_1$=120 and those for $R_2/R_1$=200 is less than 0.7%. However, the relative difference between the values at the radius ratio $R_2/R_1$=160

DOI: https://doi.org/10.1016/j.oceaneng.2018.03.079

and 200 decreases to 0.15% or below. $C_{Lrms}$ shows higher differences but the corresponding value is less than 1% for $R_2/R_1$=160 and 200. Hence, the radius ratio of 160 seems to be appropriate for the computations.

Table 1. Effect of radius ratio $R_2/R_1$ on the cylinder response and force coefficients for Re=150 and $U^*$=5.8837

| $R_2/R_1$ | $x_{0rms}$ | $y_{0rms}$ | $C_{Drms}$ | $C_{Lrms}$ |
|---|---|---|---|---|
| 120 | 0.004582 | 0.3603 | 0.2433 | 0.06760 |
| 160 | 0.004601 | 0.3608 | 0.2443 | 0.06851 |
| 200 | 0.004613 | 0.3612 | 0.2449 | 0.06912 |

For the investigation of grid independence, the number of peripheral points is chosen to be $\xi_{max}$=300, 360 and 420 while the radius ratio and dimensionless time step are fixed at $R_2/R_1$=160 and $\Delta t$=0.0005, respectively. In order to generate an equidistant grid on the computational domain, $\eta_{max}$ is chosen to be $\eta_{max}$=242, 291 and 339. Results are shown in Table 2. The highest relative differences are observed in $C_{Lrms}$: 0.65% and 0.18% between the results for $\xi_{max}$=300 and 420 and for 360 and 420, respectively. In the values of $x_{0rms}$ and $C_{Drms}$ the relative difference for $\xi_{max}$=300 and 420 is approximately 0.32%, which decreases to 0.09% for $\xi_{max}$=360 and 420. $y_{0rms}$ shows the least relative differences, which are 0.15% and 0.04% for the coarsest and the medium grid resolution, respectively.

Table 2. Grid dependence study for Re=150 and $U^*$=5.8837

DOI: https://doi.org/10.1016/j.oceaneng.2018.03.079

| $\xi_{max}$ | $x_{0rms}$ | $y_{0rms}$ | $C_{Drms}$ | $C_{Lrms}$ |
|---|---|---|---|---|
| 300 | 0.004612 | 0.3612 | 0.2449 | 0.06874 |
| 360 | 0.004601 | 0.3608 | 0.2443 | 0.06841 |
| 420 | 0.004597 | 0.3607 | 0.2441 | 0.06829 |

Finally, the effect of dimensionless time step is studied. The grid and radius ratio are fixed at 360×291 and $R_2/R_1$=160, respectively. For this investigation computations are carried out for the dimensionless time step values of 0.001 ($\Delta t_1$), 0.0005 ($\Delta t_2$) and 0.00025 ($\Delta t_3$). Here also, $C_{Lrms}$ shows the highest relative differences: 1.4% for $\Delta t_1$ and $\Delta t_3$ and 0.5% for $\Delta t_2$ and $\Delta t_3$. In the values of $x_{0rms}$ and $C_{Drms}$ the corresponding difference is around 0.3% for $\Delta t_1$ and 0.09% for $\Delta t_2$. As was observed in the grid dependence study, the relative difference is the least for $y_{0rms}$: 0.1% for $\Delta t_1$ and 0.03% for $\Delta t_2$. Thus, the time-step value of $\Delta t$=0.0005 seems to be adequate for further computations.

Table 3. Effect of dimensionless time step $\Delta t$ on the cylinder response and force coefficients for Re=150 and $U^*$=5.8837

| $\Delta t$ | $x_{0rms}$ | $y_{0rms}$ | $C_{Drms}$ | $C_{Lrms}$ |
|---|---|---|---|---|
| 0.001 | 0.004592 | 0.3606 | 0.2438 | 0.06781 |
| 0.0005 | 0.004601 | 0.3608 | 0.2443 | 0.06841 |
| 0.00025 | 0.004606 | 0.3610 | 0.2445 | 0.06875 |

### 3.2 Code validation for stationary and elastically supported cylinders

DOI: https://doi.org/10.1016/j.oceaneng.2018.03.079

The in-house code applied for the computations has been extensively tested in order to prove its accuracy (see e.g. Baranyi, 2008). For further testing, first, the flow around a stationary cylinder is investigated. Reynolds number was varied in the range of Re=80–180, where the flow is two-dimensional (Barkley and Henderson, 1999) and periodic vortex shedding occurs. In Fig. 3a rms values of lift coefficient $C_{Lrms}$ are shown against Re. Good agreement is found between our results and those of Baranyi and Lewis (2006) and Golani and Dhiman (2014). The variation of Strouhal number $St_0$ – which is the dimensionless vortex shedding frequency for a stationary cylinder – is shown in Fig. 3b. As can be seen, the current results compare well with the numerical studies of Silva et al. (2003), Baranyi and Lewis (2006), and Posdziech and Grundman (2007) and with the experimental studies of Norberg (2003).

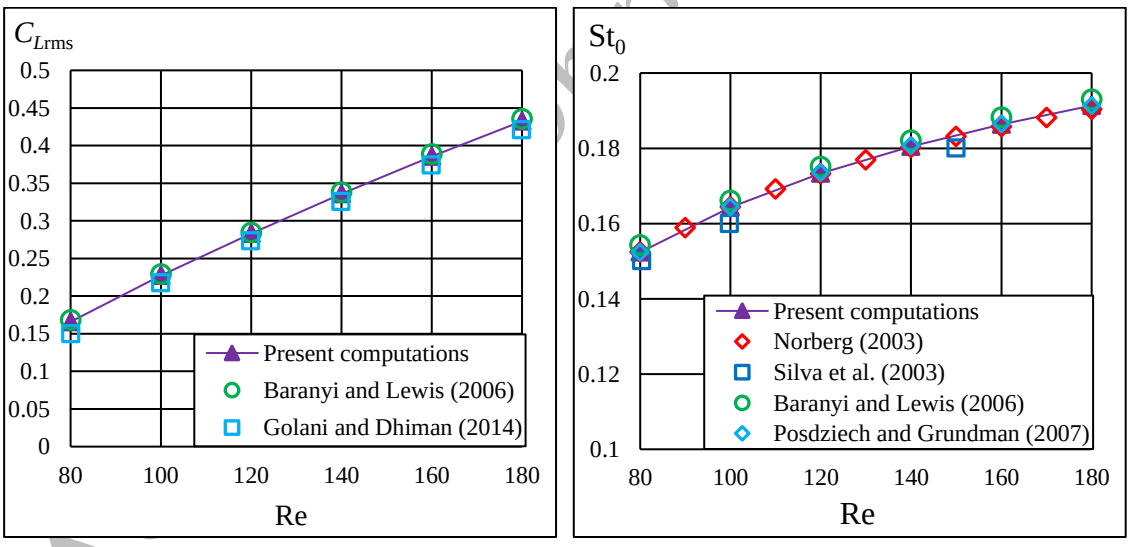


(a) $C_{Lrms}$ (b) $St_0$

Figure 3. Results for stationary cylinders: root-mean square value of lift coefficient (a) and dimensionless vortex shedding frequency (b) compared to published results

Computational results for a freely vibrating cylinder in 2DoF are shown in Fig. 4. Prasanth and Mittal (2008) and He and Zhang (2016) carried out computations where

DOI: https://doi.org/10.1016/j.oceaneng.2018.03.079

the natural frequency was kept at a constant value, which agreed with the vortex-shedding frequency for a stationary cylinder at Reynolds number $Re_0$=100. In this case the relationship between Re and $U^*$ is Re=16.6$U^*$. The mass ratio was fixed at $m^*$=10 and the structural damping coefficient was set to zero ($\zeta$=0). In Fig. 4 rms values of transverse and streamwise displacements are shown against Re. The agreement between the current results and those obtained by Prasanth and Mittal (2008) and He and Zhang (2016) is excellent except for the lower and higher threshold of flow synchronization. At the vicinity of Re=90 and 130 the flow is very sensitive to changes in the Reynolds number (and also in the reduced velocity), which explains the higher discrepancies between the results.

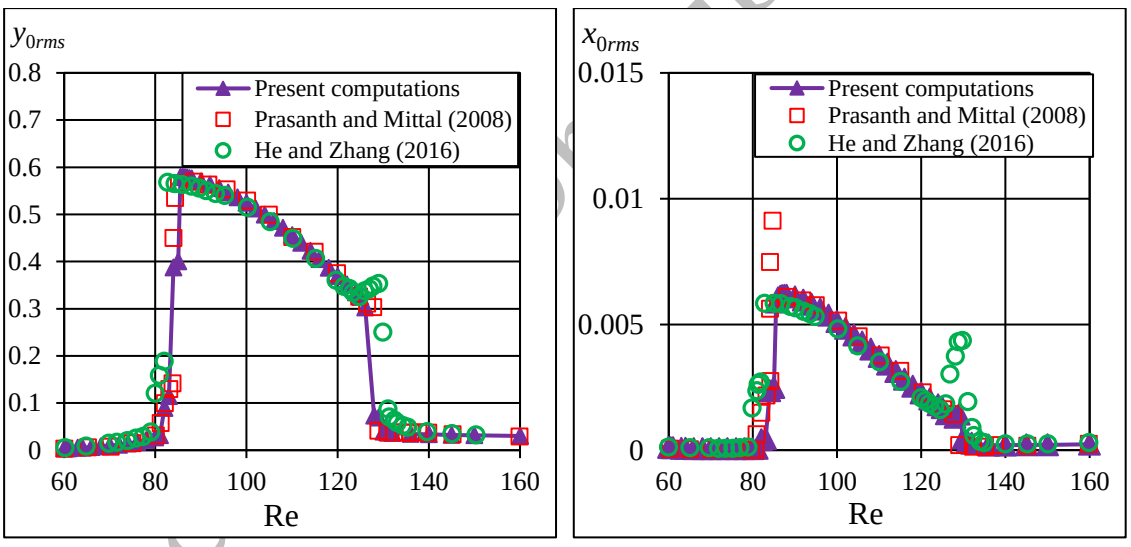


(a) $y_{0rms}$ (b) $x_{0rms}$

Figure 4. Elastically supported cylinder results: root-mean-square value of transverse (a) and streamwise displacement (b) of the cylinder compared to Prasanth and Mittal (2008) and He and Zhang (2016)

Reassuringly, 2S vortex shedding mode occurs for low transverse oscillation amplitude cases (e.g. at the initial branch) and C(2S) mode of vortex shedding is

DOI: https://doi.org/10.1016/j.oceaneng.2018.03.079

observed for high transverse cylinder displacements, similar to results obtained by Prasanth and Mittal (2008) and He and Zhang (2016).

## 4. Results and discussion

In this study flow around a circular cylinder undergoing two-degrees-of-freedom free vibration is investigated. The mass ratio is fixed at $m^*$=10 and the structural damping is chosen to be zero ($\zeta$=0) to ensure high amplitude cylinder displacement. As mentioned in Section 1, Reynolds number and reduced velocity are not independent parameters. If the natural frequency of the oscillating cylinder $f_N$ is constant, the relationship between Re and $U^*$ is linear, $Re=KU^*$ where $K=f_N D^2/\nu$=const (Mittal and Singh, 2005). Assuming that the reduced natural frequency $F_N=1/U^*$ is identical to the Strouhal number for a stationary cylinder $St_0$ at Reynolds number $Re_0$, $K$ can be determined as $K=Re_0\ St_0$.

It was found in the literature review that earlier investigations had been limited to low natural frequency values. For 2DoF motion only $Re_0$=100 was investigated (Prasanth and Mittal, 2008). In order to fill this gap, systematic computations are carried out for four different $Re_0$ values. $St_0$, $Re_0$, and the computed $K$ values are given in Table 4.

Table 4. Dimensionless vortex shedding frequencies for stationary cylinder $St_0$ and the computed constant values $K$ for different Reynolds numbers $Re_0$

| $Re_0$ | $St_0$ (Baranyi and Lewis, 2006) | $K=Re_0\ St_0$ |
|---|---|---|
| 80 | 0.1543 | 12.344 |
| 100 | 0.166 | 16.60 |
| 140 | 0.1821 | 25.494 |

DOI: https://doi.org/10.1016/j.oceaneng.2018.03.079

| | | |
|---|---|---|
| 180 | 0.193 | 34.74 |

### 4.1. Cylinder response and aerodynamic force coefficients

The root-mean-square (rms) values of the transverse cylinder displacement $y_{0rms}$ for the investigated $Re_0$ are shown in Fig. 5. As can be seen, the cylinder response for a given $Re_0$ value consists of three different regimes. At the initial branch the cylinder oscillation amplitude is low – in both streamwise and transverse directions – and the transverse vibration frequency $f_y^*$ is approximately equal to the dimensionless vortex-shedding frequency for a stationary cylinder $St_0$. In Fig. 6 the variation of $St_0$, $F_N$ and $f_y^*$ is shown for $Re_0$=140, where $f_y^* \cong St_0$ at the initial branch can be clearly seen. With increasing Re and $U^*$, cylinder response switches to the lower branch, where the oscillation frequency synchronizes with the natural frequency of the cylinder, resulting in high amplitude oscillations. Beyond the lock-in domain, the oscillation amplitude becomes small again and $f_y^*$ locks in to $St_0$, as was observed in the initial branch.



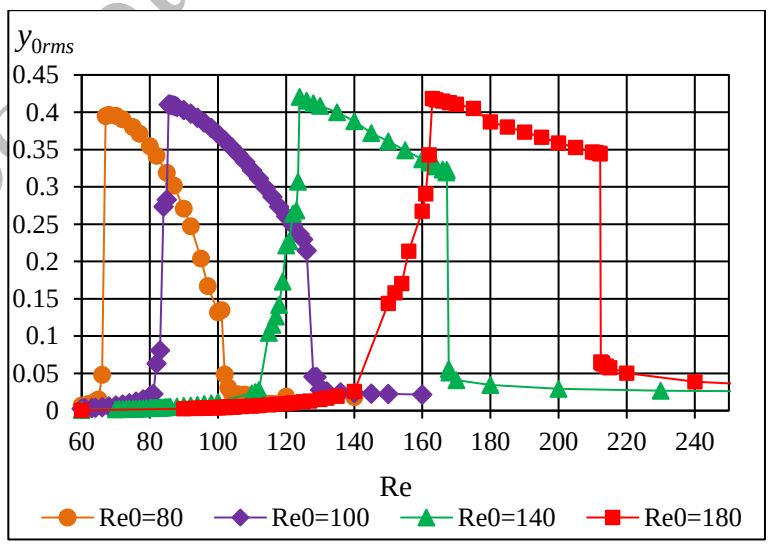

DOI: https://doi.org/10.1016/j.oceaneng.2018.03.079

Figure 5. Root-mean-square values of transverse cylinder displacement $y_{0rms}$ against Re for $Re_0$=80, 100, 140, 180

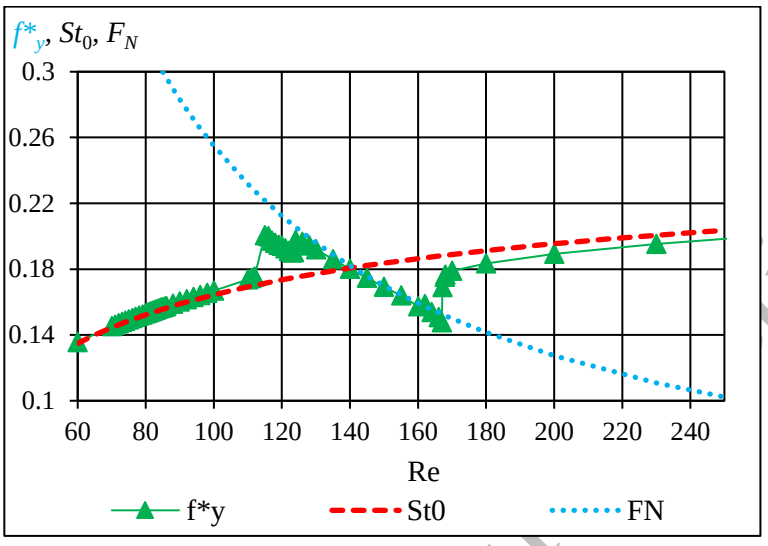


Figure 6. Dimensionless transverse vibration frequency for $Re_0$=140, dimensionless vortex-shedding frequency for stationary cylinder $St_0$ (Posdziech and Grundmann, 2007) and reduced natural frequency $F_N$ against Re

The Reynolds number range in which the oscillation frequency synchronizes with the natural frequency, i.e. lock-in, strongly depends on $Re_0$ (see Fig. 5), therefore comparison of data is difficult. Khalak and Williamson (1999) showed that the cylinder responses for different mass-damping parameters $m^*\zeta$ can collapse into a single curve by using 'true' reduced velocity ($U^*/f^*$, where $f^*$ is the ratio of the transverse oscillation frequency and the natural frequency of the cylinder) as an independent variable instead of reduced velocity. Due to $\zeta$=0, mass damping parameter is zero in all the cases investigated in this study. Singh and Mittal (2005) used $U^*St_0$ as an independent variable for the cases where either Re or $U^*$ was kept constant. Using the definitions of reduced velocity and Strouhal number, it can be seen that $U^*St_0$ is the ratio of the

DOI: https://doi.org/10.1016/j.oceaneng.2018.03.079

vortex-shedding frequency for a stationary cylinder $f_v$ and the natural frequency of the oscillating body $f_N$ ($U^*\mathrm{St}_0 = \frac{U_\infty}{f_N d}\frac{f_v d}{U_\infty} = \frac{f_v}{f_N}$). To the best knowledge of the authors, $U^*\mathrm{St}_0$ has not previously been applied as an independent variable for constant natural frequency cases. However, it can be seen in Fig. 7 that by plotting $y_{0rms}$ against $U^*\mathrm{St}_0$ the curves belonging to different $\mathrm{Re}_0$ values can be represented in the same range.

Strouhal number values in the range of Re=50–250 are obtained from Posdziech and Grundmann (2007). As can be seen in Fig. 7, the curves shift to higher $y_{0rms}$ with increasing $\mathrm{Re}_0$. A larger difference in $y_{0rms}$ values is found between $\mathrm{Re}_0$=80 and 100 than between $\mathrm{Re}_0$=140–180. It can also be seen that the lower branch is significantly wider for lower $\mathrm{Re}_0$ values. Previous researchers (e.g. Prasanth and Mittal, 2008) showed that in the transition between the initial and the lower branch – where the oscillation amplitude varies strongly – the flow is chaotic. The width of this transition range also depends on $\mathrm{Re}_0$. In the case of $\mathrm{Re}_0$=80 and 100 $y_{0rms}$ jumps abruptly between the two branches, in contrast to $\mathrm{Re}_0$=140 and 180, where the rms value of the transverse vibration component changes gradually.

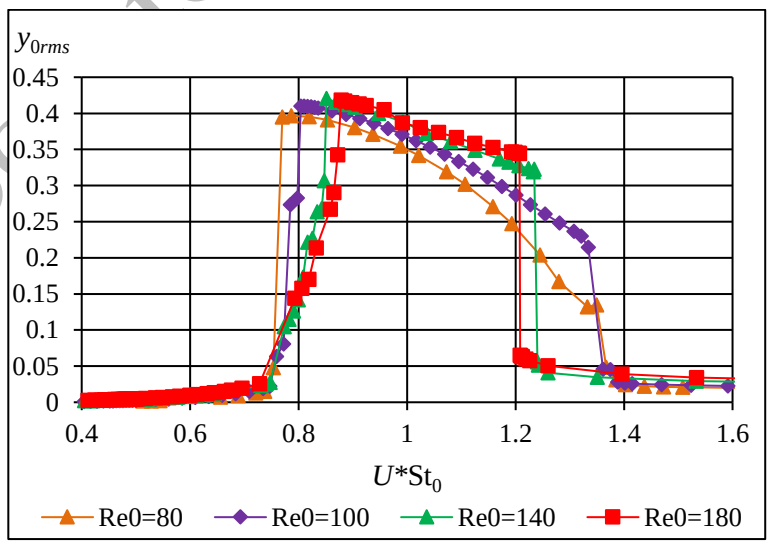

DOI: https://doi.org/10.1016/j.oceaneng.2018.03.079

Figure 7. Root-mean-square value of transverse cylinder displacement against $U^*St_0$ for $Re_0$=80, 100, 140, 180

In Fig. 8 the rms of lift coefficient $C_{Lrms}$ is plotted against $U^*St_0$. It can be seen that in the initial branch and beyond the lower branch $C_{Lrms}$ shifts to higher values with increasing $Re_0$. Besides, at the transition regime between initial and lower branches $C_{Lrms}$ increases significantly up to a peak value which increases with $Re_0$. In the lower branch $C_{Lrms}$ drops to a near-zero value.

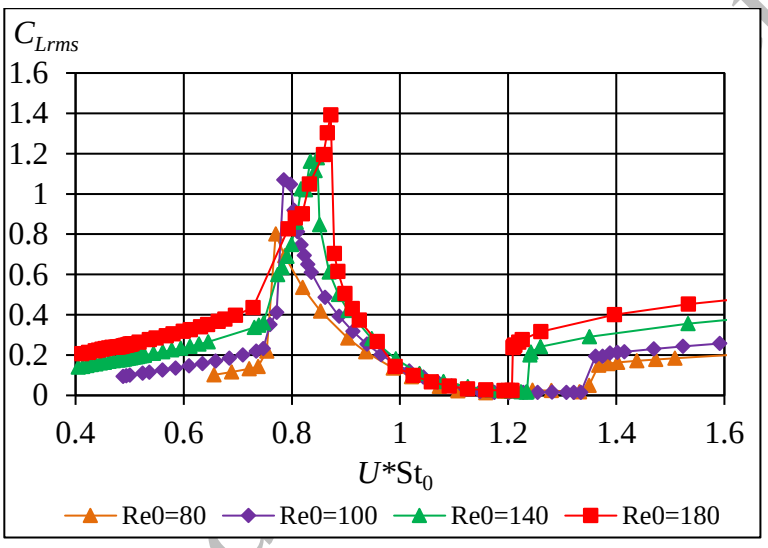


Figure 8. Root-mean-square value of lift coefficient against $U^*St_0$ for $Re_0$=80, 100, 140, 180

In Figs. 9 and 10 the rms value of the streamwise displacement $x_{0rms}$ and drag coefficient $C_{Drms}$ are shown against $U^*St_0$. As expected, the amplitude of oscillation in streamwise direction is significantly smaller than that in transverse direction. Similar characteristics are observed, as were seen for $y_{0rms}$ in Fig. 7: the curves belonging to increasing $Re_0$ shift to higher values for both $x_{0rms}$ and $C_{Drms}$. On the other hand, the rms values of streamwise cylinder displacement show an increase in the range of $U^*St_0$=0.4–0.65, which becomes more significant for higher $Re_0$ (see Fig. 9). $C_{Drms}$

DOI: https://doi.org/10.1016/j.oceaneng.2018.03.079

shows similar behavior (Fig. 10) but the difference is less than that observed in $x_{0rms}$. Note that this phenomenon is not observed for $Re_0$=80 because the flow is steady below $U^*St_0 \cong 0.5$.

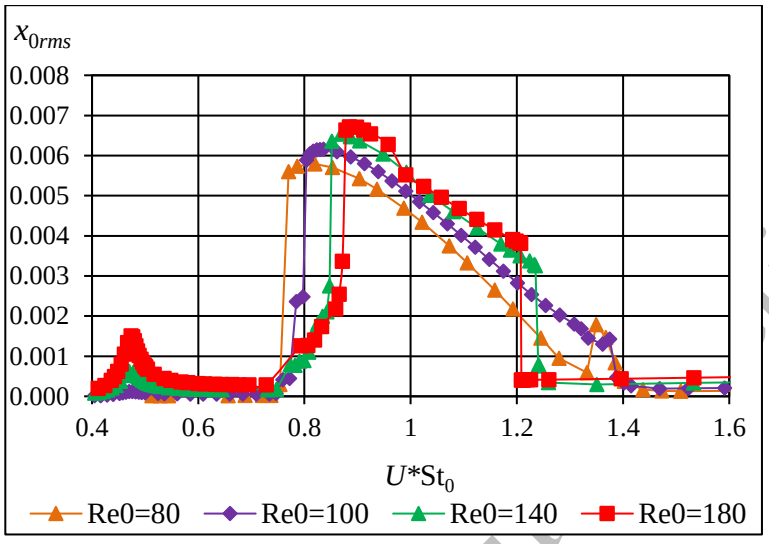


Figure 9. Root-mean-square value of streamwise cylinder displacement against $U^*St_0$ for $Re_0$=80, 100, 140, 180

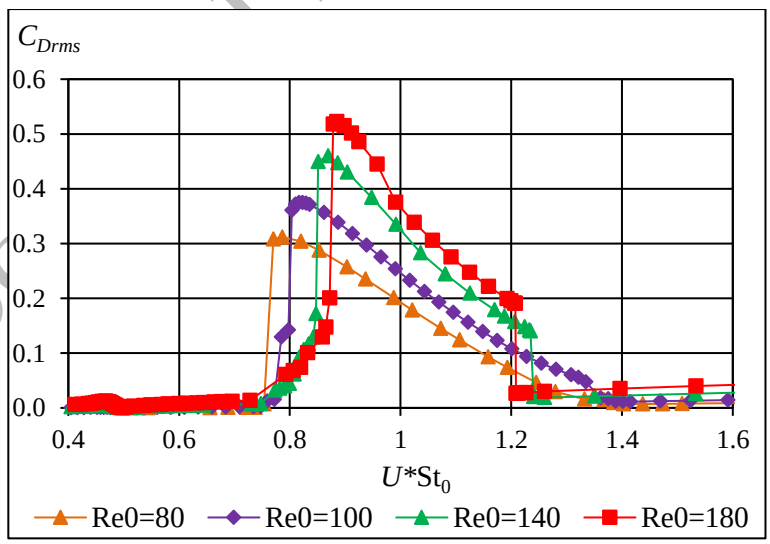


Figure 10. Root-mean-square value of drag coefficient against $U^*St_0$ for $Re_0$=80, 100, 140, 180

DOI: https://doi.org/10.1016/j.oceaneng.2018.03.079

In Fig. 11 the domain $U^*St_0$=0.4–0.65 is shown at higher resolution. It can be seen that $x_{0rms}$ increases continuously until it reaches its local maximum value at around $U^*St_0$~0.47 (see Fig. 11a). As expected, with decreasing $Re_0$ the peak value diminishes, and almost disappears at $Re_0$=100. In addition to the peak, a local minimum point is identified for $C_{Drms}$ at $U^*St_0 \cong 0.5$ where it approaches zero (see Fig. 11b). After the local minimum point $C_{Drms}$ starts to increase, with the slope of the curve increasing with $Re_0$. To check the significance of the local maximum values of $x_{0rms}$ and $C_{Drms}$ and local minimum values of $C_{Drms}$, the domain $U^*St_0$=0.4–0.65 is further investigated.

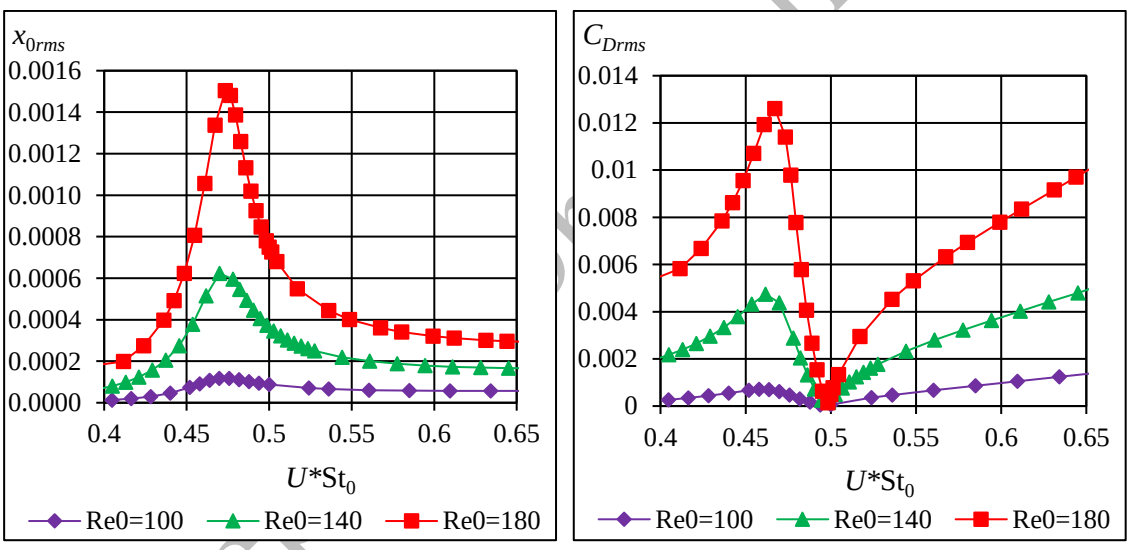


(a) $x_{0rms}$ (b) $C_{Drms}$

Figure 11. Root-mean-square value of streamwise cylinder displacement (a) and drag coefficient (b) against $U^*St_0$ (zoom-in) for $Re_0$=100, 140, 180

## 4.2. Investigating the vicinity of $U^*St_0$=0.5

In order to investigate the significance of local maximum points identified in $x_{0rms}$ and $C_{Drms}$ and local minimum point found in $C_{Drms}$, the phase angle $\Phi$ between $x_0$ and $C_D$ is computed. Figure 12 shows $C_{Drms}$ against $U^*St_0$ for $Re_0$=180 (Fig. 12c) and time

DOI: https://doi.org/10.1016/j.oceaneng.2018.03.079

histories of drag coefficient and streamwise cylinder displacement (Fig. 12a, b, d, e) for different $U^*St_0$ values. It can be seen in the figure that there is an irregular change in the phase difference between $x_0$ and $C_D$ at around $U^*St_0=0.5$. At $U^*St_0 < 0.5$ $x_0$ and $C_D$ are in phase, so the phase angle between the signals is $\Phi \cong 0°$ and in the vicinity of $U^*St_0=0.5$ (when $C_{Drms}$ approaches zero) the phase angle jumps to $\Phi=180°$.

DOI: https://doi.org/10.1016/j.oceaneng.2018.03.079

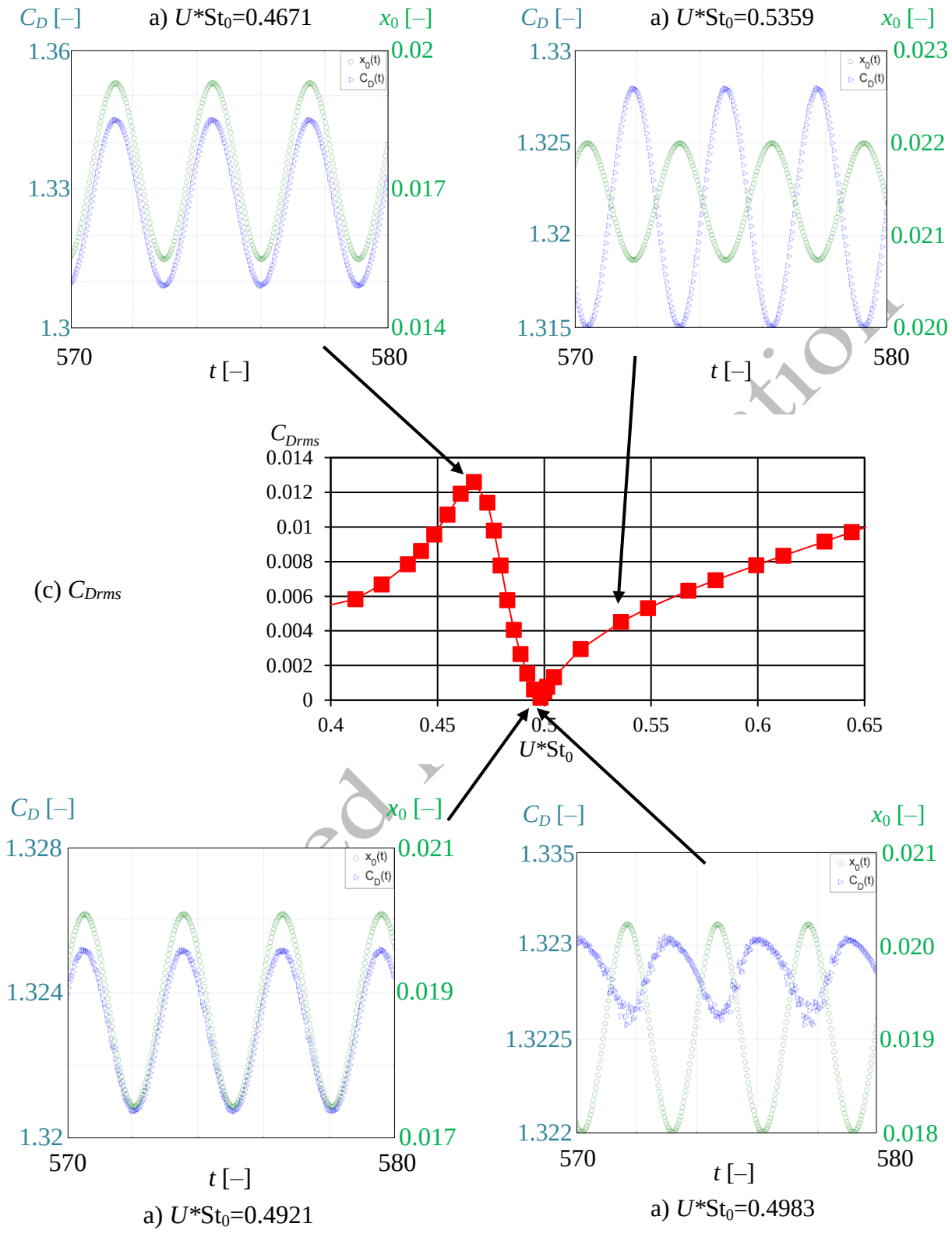


Figure 12. Time histories of drag coefficient (blue triangular marker) and streamwise cylinder displacement (green circular marker) belonging to different $U$*St$_0$ values

DOI: https://doi.org/10.1016/j.oceaneng.2018.03.079

The phase angle $\Phi$ computed using Hilbert transformation is shown in Fig. 13 against $U^*St_0$ for the investigated $Re_0$ values. The jump in the phase between 0° and 180° can be clearly seen.

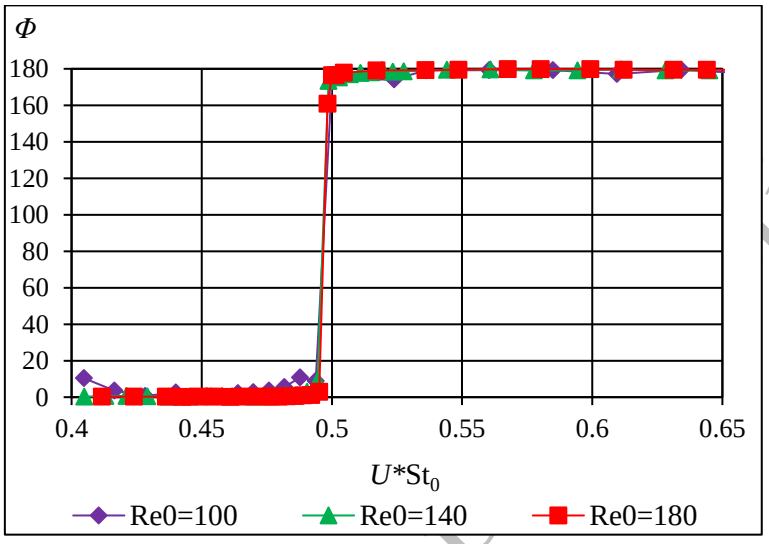


Figure 13. Phase angle between $x_0$ and $C_D$ against $U^*St_0$ for $Re_0$=100, 140, 180

The total drag coefficient is composed of two parts: one is due to pressure $C_{Dp}$ and another part originating from friction on the cylinder wall $C_{Dv}$, as stated by Eq. (9). The rms values of $C_{Dp}$ and $C_{Dv}$ in the range $U^*St_0$=0.4–0.65 show different behaviors, as can be seen in Fig. 14. Although both quantities have maximum and minimum values in this range, the variation of $C_{Dprms}$ is similar to $C_{Drms}$ (Fig. 11b), while the change in $C_{Dvrms}$ is similar to the characteristics of $x_{0rms}$ (Fig. 11a).

DOI: https://doi.org/10.1016/j.oceaneng.2018.03.079

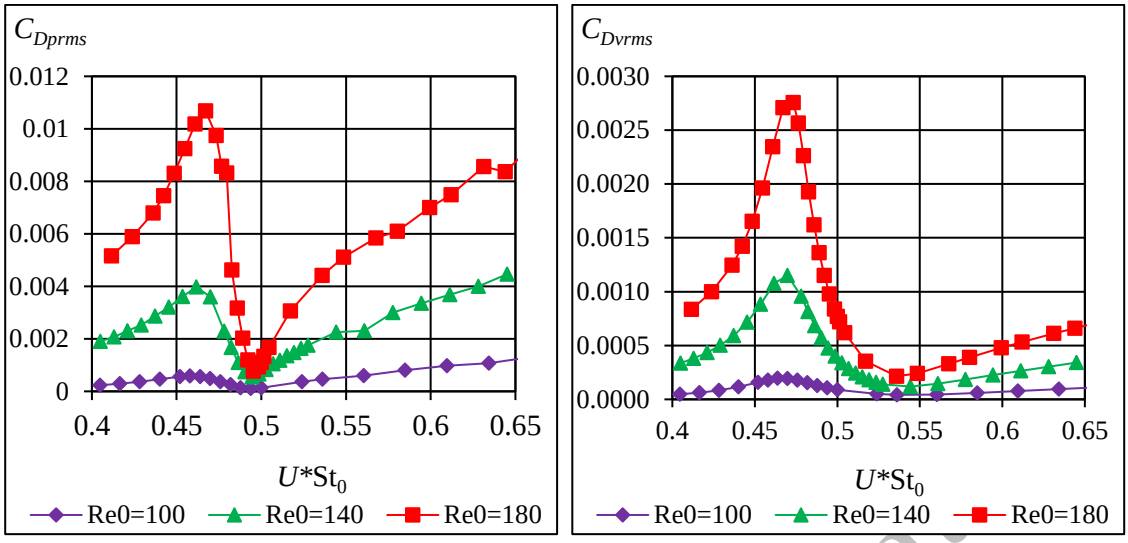


(a) $C_{Dprms}$ (b) $C_{Dvrms}$

Figure 14. Root-mean-square values of drag due to pressure (a) and drag due to viscosity (b) against $U$*St$_0$ for Re$_0$=100, 140, 180

For this reason $\Phi_v$ (phase angle between $C_{Dv}$ and $x_0$) and $\Phi_p$ (phase angle between $C_{Dp}$ and $x_0$) are computed and shown for the investigated Re$_0$ values in Fig. 15. As expected, the changes in $\Phi_v$ and $\Phi_p$ are different. In the range of $U$*St$_0$≅0.4–0.5 there is a $\Phi_v$≅35° phase shift between $C_{Dv}$ and $x_0$. After this period $\Phi_v$ changes gradually until it reaches approximately 180° (see Fig. 15b). In contrast, $C_{Dp}$ and $x_0$ are approximately in phase between $U$*St$_0$=0.4 and 0.5, while in the vicinity of $U$*St$_0$=0.5 the phase angle changes abruptly to $\Phi_p$=180° (see Fig. 15a).

The tendencies of $\Phi_p$ and $\Phi$ are very similar (see Figs. 15a and 13), therefore pressure distribution around the cylinder surface influences the flow structure more strongly than friction does. This behavior is similar to that observed by Prasanth and Mittal (2008) for Re$_0$=100, who found an abrupt jump in the phase between the lift coefficient and transverse displacement from $\Phi$=0° to 180° (between Re=110 and 115). Decomposing lift into pressure lift $C_{Lp}$ and viscous lift $C_{Lv}$ they showed that the pressure

DOI: https://doi.org/10.1016/j.oceaneng.2018.03.079

component is responsible for the jump, since the viscous component remains in phase with the displacement.

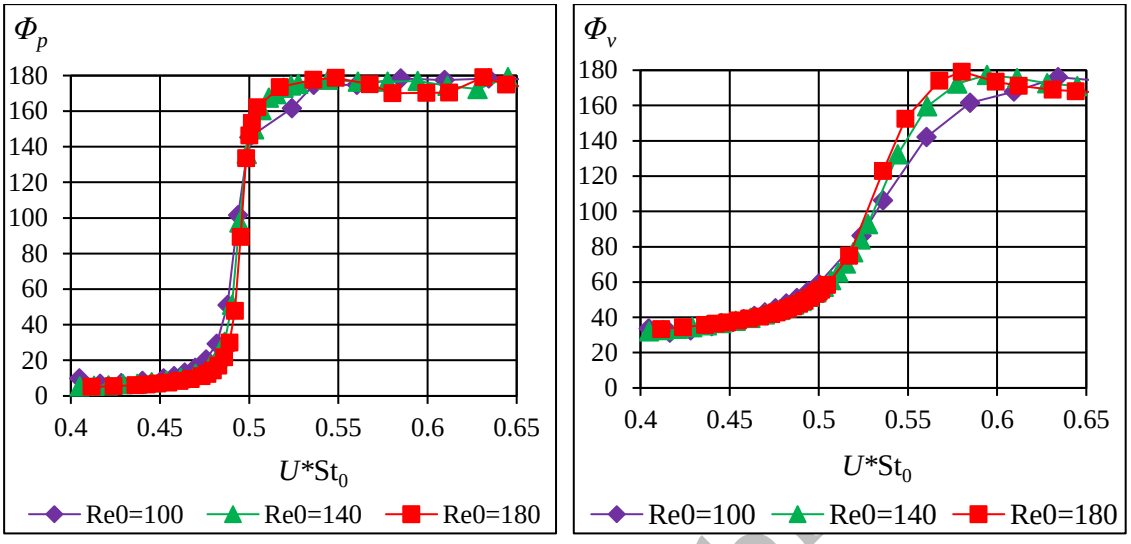


(a) $\phi_p$ (b) $\phi_v$

Figure 15. Phase angle values $\Phi_v$ (a) and $\Phi_p$ (b) against $U$*St$_0$ for Re$_0$=100, 140, 180

In Fig. 16 limit cycle curves (time histories of viscous drag versus those of pressure drag) are shown for the vicinity of $U$*St$_0$=0.5 for Re$_0$=140. It can be seen that below $U$*St$_0$≅0.4904 the orientation of the curves is clockwise, indicated by filled arrows (see Fig. 16). At $U$*St$_0$ > 0.4904 the orientation switches abruptly to counterclockwise direction (shown by empty arrows in Fig. 16), which means that pressure and viscous drag become nearly antiphase. This substantial change is mainly caused by pressure drag, since $\Phi_v$ increases gradually in this regime (Fig. 15b) in contrast to $\Phi_p$, which jumps abruptly between $\Phi_p$=0° and 180° at around $U$*St$_0$=0.5 (Fig. 15a). The amplitudes of signals $C_{Dp}$ and $C_{Dv}$ (not shown here) are almost identical in the vicinity of $U$*St$_0$=0.5. These two features (antiphase and equal signal amplitudes) nearly cancel each other out, resulting in an approximately zero value of $C_{Drms}$ (shown in Fig. 11b).

DOI: https://doi.org/10.1016/j.oceaneng.2018.03.079

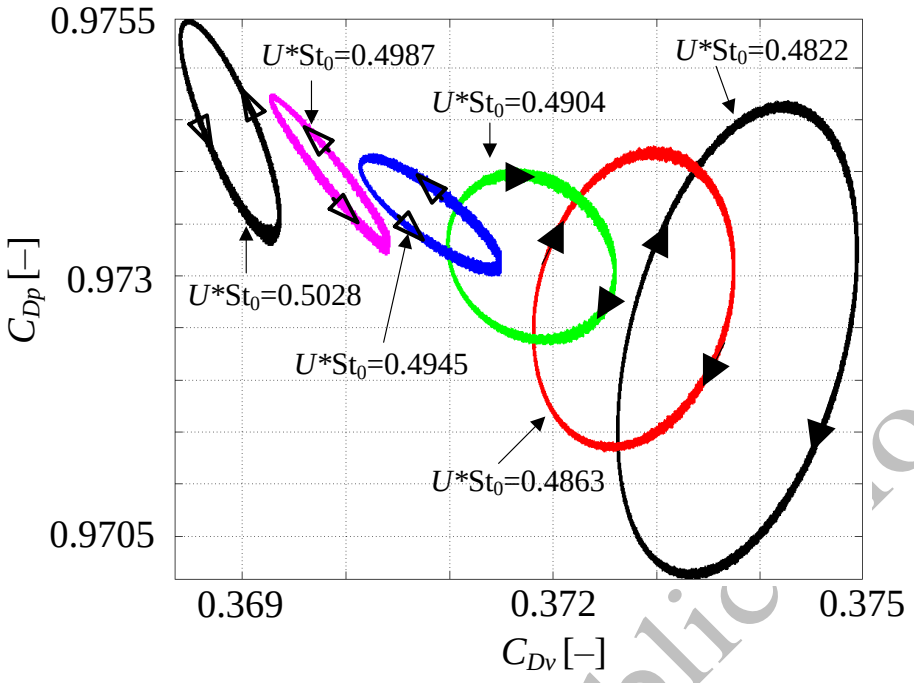


Figure 16. Limit cycle curves ($C_{Dv}$, $C_{Dp}$) in the vicinity of $U$*St$_0$=0.5 for Re$_0$=140

The abrupt change in the limit cycle curves shown in Fig. 16 suggests that the path of the cylinder also changes strongly in this domain. Figure 17 shows the power spectra (FFT) of the $x$ and $y$ components of the cylinder displacement for $U$*St$_0$=0.9246 and Re$_0$=180. The intensity value $I$ on the vertical axis is normalized by its maximum value $I_{max}$. It can be seen in the figure that the vibration frequency in the streamwise direction is double that in the transverse direction ($f_x^*=2f_y^*$), which is true for all of the investigated cases except in the chaotic flow regime.

DOI: https://doi.org/10.1016/j.oceaneng.2018.03.079

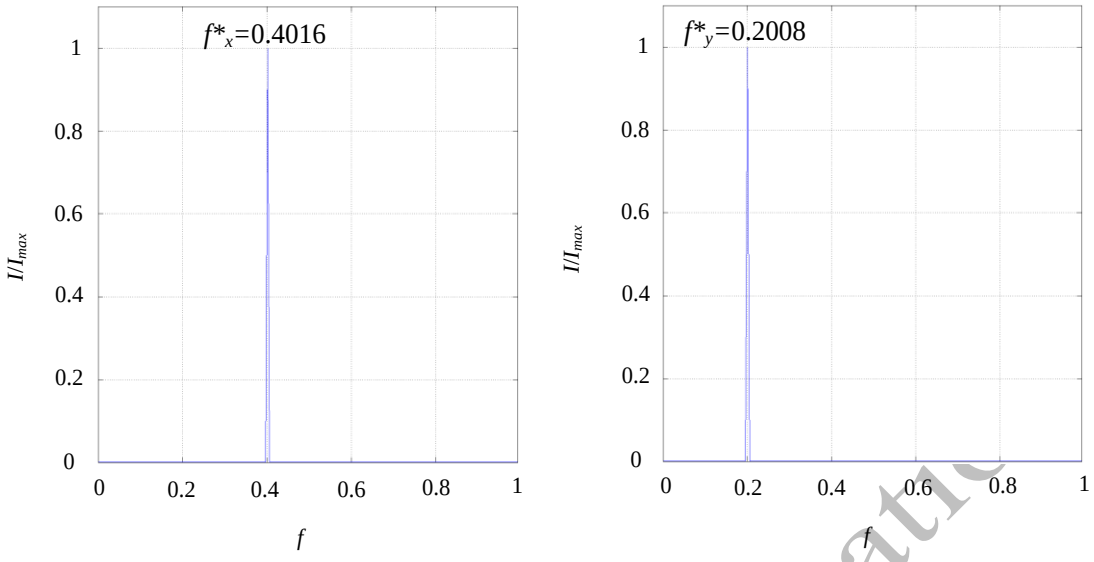


(a) $f_x^*$ (b) $f_y^*$

Figure 17. Power spectra of streamwise (a) and transverse (b) components of cylinder response for $U^*St_0=0.9246$ and $Re_0=180$

These peak values result in a distorted figure-eight (or Lissajou curve) cylinder path that can be written mathematically as follows:

$$x_0(t) = x_{0max}\cos\left(4\pi f_x^* t + \Theta\right), \tag{15}$$

$$y_0(t) = y_{0max}\sin\left(2\pi f_y^* t\right), \tag{16}$$

where $\Theta$ is the phase angle between $x$ and $y$ vibration components. Phase angle $\Theta$ determines both the shape and the orientation of the moving trajectory. In case of $\Theta > 0$ the orbit is clockwise (CW) in the upper loop of the cylinder path, while with $\Theta < 0$ values counterclockwise (CCW) cylinder paths are obtained. Eqs. (15) and (16) do not satisfy in the transition regime between initial and lower branches, where the cylinder motion is not quasi-periodic. In Fig. 18 the direction of cylinder orbit is shown for CW (filled arrows) and CCW (empty arrows) for the intersection of a distorted figure-eight path.

DOI: https://doi.org/10.1016/j.oceaneng.2018.03.079

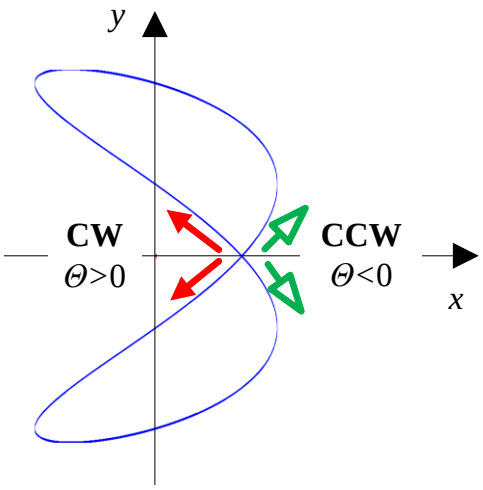


Figure 18. Direction of cylinder orbit (CW – clockwise, CCW – counterclockwise) for a distorted figure-eight path

Phase angles between the two oscillation components are computed and plotted against $U^*St_0$ for the investigated $Re_0$ values in Fig. 19. It can be seen that CW cylinder motion occurs in the approximate range of $U^*St_0$=0.4–0.5 and CCW orbits are found above $U^*St_0 \cong 0.5$. It is obvious from the figure that $\Theta$ varies strongly at the vicinity of $U^*St_0$=0.5. In Fig. 20 cylinder trajectories are shown for various $U^*St_0$ values for $Re_0$=180. It can be seen that by increasing $U^*St_0$ the phase angle sharply decreases, approaching zero at $U^*St_0 \cong 0.487$ at the same value at which the local minimum value was identified in $C_{Drms}$ (see also Fig. 11b).

DOI: https://doi.org/10.1016/j.oceaneng.2018.03.079

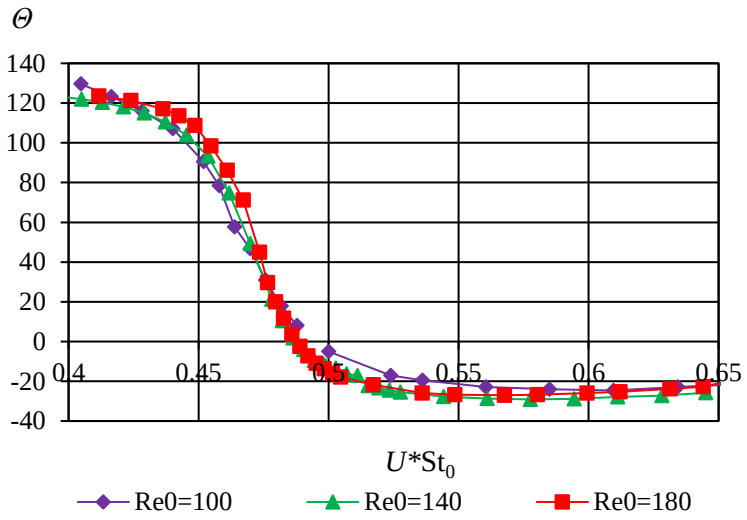


Figure 19. Phase angle $\Theta$ between streamwise and transverse components of the motion for $Re_0$=100, 140, 180

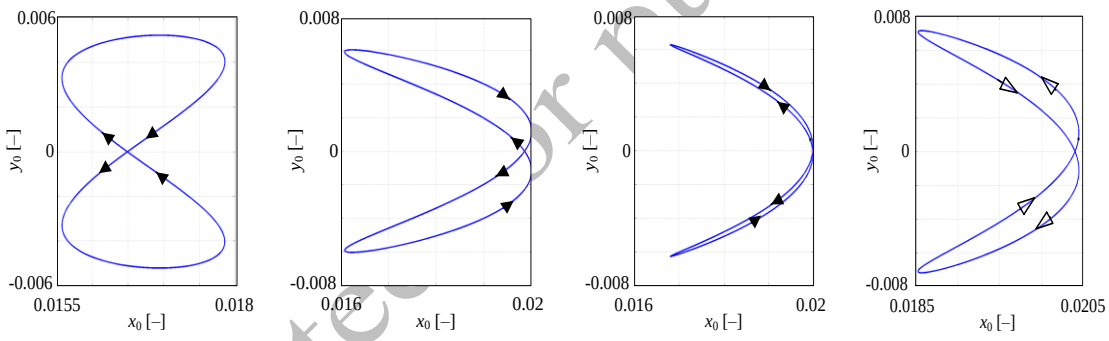


(a) $U$*St$_0$=0.455 $\Theta$=98.47° (CW)

(b) $U$*St$_0$=0.48 $\Theta$=19.91° (CW)

(c) $U$*St$_0$=0.486 $\Theta$=3.59° (CW)

(d) $U$*St$_0$=0.505 $\Theta$=-17.87° (CCW)

Figure 20. Cylinder path in the vicinity of $U$*St$_0$≅0.5 for $Re_0$=180



## 5. Conclusions

The present study deals with the numerical simulation of low-Reynolds-number flow around an elastically supported circular cylinder free to move in two directions. The

DOI: https://doi.org/10.1016/j.oceaneng.2018.03.079

mass ratio is fixed at $m^*$=10 and the structural damping coefficient is set to zero. The natural frequency of the structure $f_N$ is kept at a constant value agreeing with the vortex shedding frequency from a stationary cylinder at Reynolds numbers $Re_0$=80, 100, 140 and 180. In order to keep $f_N$ constant, both Re and reduced velocity $U^*$ are varied.

The main findings are as follows:

- A two-branch cylinder response is observed, similarly to the previously published numerical and experimental results for low-Reynolds-number flows;
- The Reynolds number range where synchronization (or lock-in) takes place strongly depends on $Re_0$, making comparison of results belonging to different natural frequencies more difficult. By plotting the results belonging to different $Re_0$ against $U^*St_0$ the data series can be represented in the same range, making comparison easier;
- With increasing $Re_0$ the root-mean-square (rms) values of cylinder displacement and drag coefficient shift to higher values and the lock-in domain becomes narrower;
- In the initial branch local extreme values are observed in the rms of streamwise displacement ($x_{0rms}$, maximum) and drag coefficient ($C_{Drms}$ maximum and minimum) in the range of $U^*St_0$=0.4–0.65;
- At $U^*St_0 \cong 0.5$ $C_{Drms}$ approaches zero. At this point the phase angle between streamwise displacement and drag coefficient changes abruptly from 0° to 180° (from in-phase to antiphase);
- Phase angles between the $x$ component of the cylinder motion and pressure and viscous drag coefficients ($\Phi_p$ and $\Phi_v$) are also computed. Although $\Phi_p$ shows a sudden shift between 0° and 180°, $\Phi_v$ gradually varies between $\Phi_v \cong 35°$ and

DOI: https://doi.org/10.1016/j.oceaneng.2018.03.079

180°. This result indicates that pressure drag may be responsible for the abrupt phase change and switch in orientation of the cylinder path;

- Due to the abrupt change in $\Phi_p$, the limit cycle curves ($C_{Dv}$, $C_{Dp}$) switch from clockwise to anticlockwise orientation in the vicinity of $U^*St_0=0.5$.
- The cylinder follows a distorted figure-eight path in all of the investigated cases except within the chaotic flow regime. The phase angle between $x$ and $y$ components of the motion is computed and used to identify the orientation of the path. It is found that at $U^*St_0 \cong 0.5$ the orientation of the cylinder path changes from a clockwise to a counterclockwise orbit.

It is seen from the current study that higher $Re_0$ values cause noticeable changes in $x_{0rms}$ and $C_{Drms}$. We plan to investigate the effect of mass ratio (at the range of $m^*=0.1$–25) on the cylinder response for higher $Re_0$ values ($Re_0 \geq 180$).

## Acknowledgements

This research was supported by the European Union and the Hungarian State, co-financed by the European Regional Development Fund in the framework of the GINOP-2.3.4-15-2016-00004 project, aimed to promote the cooperation between the higher education and the industry. The research was also supported by the EFOP-3.6.1-16-00011 “Younger and Renewing University – Innovative Knowledge City – institutional development of the University of Miskolc aiming at intelligent specialisation” project implemented in the framework of the Széchenyi 2020 program. The realization of this project is supported by the European Union, co-financed by the European Social Fund.

DOI: https://doi.org/10.1016/j.oceaneng.2018.03.079

## References

Al-Mdallal, Q.M., Lawrence, K.P., Kocabiyik, S., 2007. Forced streamwise oscillations of a circular cylinder: Locked-on modes and resulting fluid forces. *Journal of Fluids and Structures* **23** (5), 681–701.

Bahmani, M.H., Akbari, M.H., 2010. Effect of mass and damping ratios on VIV of a circular cylinder. *Ocean Engineering* **37** (5-6), 511–519.

Baranyi, L., 2008. Numerical simulation of flow around an orbiting cylinder at different ellipticity values. *Journal of Fluids and Structures* **24** (6), 883–906.

Baranyi, L., Daróczy, L., 2013. Mechanical energy transfer and flow parameter effects for a cylinder in transverse oscillation. *International Journal of Heat and Fluid Flow* **43**, 251–258.

Baranyi, L., Lewis, R.I., 2006. Comparison of grid-based CFD method and vortex dynamics predictions of low Reynolds number cylinder flows. *The Aeronautical Journal* **110**, 63–71.

Barkley, D., Henderson, R.D., 1996. Three dimensional Floquet stability analysis of the wake of a circular cylinder. *Journal of Fluid Mechanics* **322**, 215–241.

Bearman, P.W., 1984. Vortex shedding from oscillating bluff bodies. *Annual Review of Fluid Mechanics* **16**, 195–222.

Bearman, P.W., 2011. Circular cylinder wakes and vortex-induced vibrations. *Journal of Fluids and Structures* **27** (5-6), 648–658.

Bearman, P.W., Obasaju, E.D., 1982. An experimental study of pressure fluctuations fixed and oscillating square-section cylinders. *Journal of Fluid Mechanics* **119**, 297–321.

Bernitsas, M.M., Raghavan, K., Garcia, E.M.H., 2008. VIVACE (Vortex Induced Vibration Aquatic Clean Energy): a new concept in generation of clean and renewable energy from fluid flow. *Journal of Offshore Mechanics and Arctic Engineering* **130** (4), paper No. 041101, pp. 1–15.

DOI: https://doi.org/10.1016/j.oceaneng.2018.03.079

Bernitsas, M.M., Ben-Simon, Y., Raghavan, K., Garcia, E.M.H., 2009. The VIVACE converter: model tests at high damping and Reynolds number around $10^5$. *Journal of Offshore Mechanics and Arctic Engineering* **131** (1), paper No. 011102, pp. 1–12.

Bishop, R.E.D., Hassan, A.Y., 1964. The lift and drag forces on a circular cylinder oscillating in a flowing fluid. *Proc. Royal Society of London*, Series A. **277** (1368), 51–75.

Blevins, R.D., 1990. Flow-Induced Vibration. Van Nostrand Reinhold Co., Inc., New York, NY, USA

Brika, D., Laneville, A., 1993. Vortex-induced vibration of a long flexible circular cylinder. *Journal of Fluid Mechanics* **250**, 481–508.

Dahl, J.M., Hover, F.S., Triantafyllou, M.S., 2006. Two-degree-of-freedom vortex-induced vibrations using a force assisted apparatus. *Journal of Fluids and Structures* **22** (6-7), 807–818.

Feng, CC., 1968. The measurement of vortex-induced effects in flow past stationary and oscillating circular and D-section cylinders. Master thesis, University of British Columbia, Vancouver, B.C., Canada

Golani, R., Dhiman, A.K., 2014. Fluid flow and heat transfer across a circular cylinder in the unsteady flow regime. *The International Journal of Engineering and Sciences* **3** (3), 8–19.

Govardhan, R., Williamson, C.H.K., 2000. Modes of vortex formation and frequency response for a freely-vibrating cylinder. *Journal of Fluid Mechanics* **420**, 85–110.

Govardhan, R.N., Williamson, C.H.K., 2006. Defining the 'modified Griffin plot' in vortex-induced vibration: revealing the effect of Reynolds number using controlled damping. *Journal of Fluid Mechanics* **561**, 147–180.

Harlow, F.H., Welch, J.E., 1965. Numerical calculation of time-dependent viscous incompressible flow of fluid with free surface. *Physics of Fluids* **8** (12), 2182–2189.

He, T., Zhang, K., 2016. An overview of the combined interface boundary condition method for fluid-structure interaction. Proc. *Archives of Computational Methods in Engineering*, Barcelona, Spain, pp. 1–44.

DOI: https://doi.org/10.1016/j.oceaneng.2018.03.079

Jauvtis, N., Williamson, C.H.K., 2004. The effect of two degrees of freedom on vortex-induced vibration at low mass and damping. *Journal of Fluid Mechanics* **509**, 23–62.

Jeon, D., Gharib, M., 2001. On circular cylinders undergoing two-degree-of-freedom forced motions. *Journal of Fluids and Structures* **15** (3-4), 533–541.

Kaiktsis, L., Triantafyllou, G.S., Özbas, M., 2007. Excitation, inertia, and drag forces on a cylinder vibrating transversely to a steady flow. *Journal of Fluids and Structures* **23** (1), 1–21.

Kang, Z., Ni, W., Sun, L., 2016. An experimental investigation of two-degree-of-freedom VIV trajectories of a cylinder at different scales of natural frequency ratios. *Ocean Engineering* **126**, 187–202.

Kawamura, T., Takami, H., Kuwahara, K., 1986. Computation of high Reynolds number flow around a circular cylinder with surface roughness. *Fluid Dynamics Research* **1** (2), 145–162.

Khalak, A., Williamson, C.H.K., 1999. Motions, forces and mode transitions in vortex-induced vibrations at low mass-damping. *Journal of Fluids and Structures* **13** (7-8), 813–851.

Klamo, J.T., Leonard, A., Roshko, A., 2006. The effect of damping on the amplitude and frequency response of a freely vibrating cylinder in cross-flow. *Journal of Fluids and Structures* **22** (6-7), 845–856.

Koide, M., Tomida, S., Takahashi, T., Baranyi, L., Shirakashi, M., 2002. Influence of cross-sectional configuration on the synchronization of Kármán vortex shedding with the cylinder oscillation. *JSME International Journal, Series B* **45** (2), 249–258.

Leontini, J.S., Thompson, M.C., Hourigan, K., 2006. The beginning of branching behavior of vortex-induced vibration during two-dimensional flow. *Journal of Fluids and Structures* **22** (6-7), 857–864.

Lu, X.Y., Dalton, C., 1996. Calculation of the timing of vortex formation from an oscillating cylinder. *Journal of Fluids and Structures* **10** (5), 527–541.

DOI: https://doi.org/10.1016/j.oceaneng.2018.03.079

Mehmood, A., Abdelkefi, A., Hajj, M.R., Nayfeh, A.H., Akhtar, I., Nuhait, A.O., 2013. Piezoelectric energy harvesting from vortex-induced vibrations of a circular cylinder. *Journal of Sound and Vibration* **332** (19), 4656–4667.

Meneghini, J.R., Bearman, P.W., 1997. An investigation of the effect on vortex shedding of a sudden transverse disturbance applied to a circular cylinder. *Journal of Wind Engineering and Industrial Aerodynamics* **69-71**, 229–238.

Mittal, S., Singh, S., 2005. Vortex-induced vibrations at subcritical Re. *Journal of Fluid Mechanics* **534**, 185–194.

Moe, G., Wu, Z.-J., 1990. The lift force on a cylinder vibrating in a current. *Journal of Offshore Mechanics and Arctic Engineering* **112** (4), 297–303.

Mureithi, N.W., Huynh, K., Rodriguez, M., Pham, A., 2010. A simple low order model of forced Karman wake. *International Journal of Mechanical Sciences* **52** (11), 1522–1534.

Nakamura, T., Kaneko, S., Inada, F., Kato, M., Ishihara, K., Nishihara, T., Mureithi, N.W., Langthjem, M.A., 2013. Flow-induced Vibration: Classifications and Lessons from Practical Experiences. Butterworth-Heinemann, London

Nishihara, T., Kaneko, S., Watanabe, T., 2005. Characteristics of fluid dynamic forces acting on a circular cylinder oscillated in the streamwise direction and its wake patterns. *Journal of Fluids and Structures* **20** (4), 505–518.

Norberg, C., 2003. Fluctuating lift on a circular cylinder: review and new measurements. *Journal of Fluids and Structures* **17** (1), 57–96.

Okajima, A., Nakamura, A., Kosugi, T., Uchida, H., Tamaki, R., 2004. Flow-induced in-line oscillation of a circular cylinder. *European Journal of Mechanics B/Fluids* **23** (1), 115–125.

Peppa, S., Kaiksis, L., Triantafyllou, G.S., 2016. Hydrodynamic forces and flow structures in flow past a cylinder forced to vibrate transversely and inline to a steady flow. *Journal of Offshore Mechanics and Arctic Engineering* **138** (1), Paper No: OMAE–14–1134

Poncet, P., 2002. Vanishing of mode B in the wake behind a rotationally oscillating circular cylinder. *Physics of Fluids* **14** (6), 2021–2023.

DOI: https://doi.org/10.1016/j.oceaneng.2018.03.079

Posdziech, P., Grundmann, R., 2007. A systematic approach to the numerical calculation of fundamental quantities of the two-dimensional flow over a circular cylinder. *Journal of Fluids and Structures* **23** (3), 479–499.

Prasanth, T.K., Behara, S., Singh, S.P., Kumar, R., Mittal, S., 2006. Effect of blockage on vortex-induced vibrations at low Reynolds numbers. *Journal of Fluids and Structures* **22** (6-7), 865–876.

Prasanth, T.K., Mittal, S., 2008. Vortex-induced vibrations of a circular cylinder at low Reynolds numbers. *Journal of Fluid Mechanics* **594**, 463–491.

Sanchis, A., 2009. Two degrees of freedom vortex-induced vibrations of a rigid circular cylinder with varying natural frequencies in the x and y directions. Proc. ASME 2009 28th International Conference on Ocean, Offshore and Arctic Engineering, Honolulu, Hawaii, USA, pp. 889–894.

Sarpkaya, T., 1995. Hydrodynamic damping, flow-induced oscillations, and biharmonic response. *Journal of Offshore Mechanics and Arctic Engineering* **117** (4), 232–238.

Sarpkaya, T., 2004. A critical review of the intrinsic nature of the vortex-induced vibrations. *Journal of Fluids and Structures* **19** (4), 389–447.

Silva, L.E.A.L.F., Neto, S.A., Damasceno, J.J.R., 2003. Numerical simulation of two-dimensional flows over a circular cylinder using the immersed boundary method. *Journal of Computational Physics* **189** (2), 351–370.

Singh, S.P., Mittal, S., 2005. Vortex-induced oscillations at low Reynolds numbers: hysteresis and vortex-shedding modes. *Journal of Fluids and Structures* **20** (8), 1085–1104.

Stansby, P.K., Rainey, R.C.T., 2001. A CFD study of the dynamic response of a rotating cylinder in a current. *Journal of Fluids and Structures* **15** (3-4), 513–521.

Tang, G., Lu, L., Zhao, M., Liu, M., Zong, Z., 2017. Phase jump and energy transfer of forced oscillating circular cylinder in uniform flow. *Proc. of the Institution of Mechanical Engineers, Part M: Journal of Engineering of the Maritime Environment* **231** (2), 496–510

DOI: https://doi.org/10.1016/j.oceaneng.2018.03.079

Thompson, M.C., Le Gal, P., 2004. The Stuart-Landau model applied to wake transition revisited. *European Journal of Mechanics – B/Fluids* **23** (1), pp. 219–228.

Willden, R.H.J., Graham, J.M.R., 2006. Three distinct response regimes for transverse vortex-induced vibrations of circular cylinders at low Reynolds numbers. *Journal of Fluids and Structures* **22** (6-7), 885–895.

Williamson, C.H.K, Govardhan, R., 2004. Vortex-induced vibration. *Annual Review of Fluid Mechanics* **36**, 413–455.

Williamson, C.H.K., Roshko, A., 1988, Vortex formation in the wake of an oscillating cylinder. *Journal of Fluids and Structures* **2** (4), 355–381.

Zhou, C.Y., So, C., Lam, K., 1999. Vortex-induced vibrations of an elastic circular cylinder. *Journal of Fluids and Structures* **13** (2), 165–189.

DOI: https://doi.org/10.1016/j.oceaneng.2018.03.079

## Figure captions

Figure 1. Layout of the elastically supported cylinder

Figure 2. The physical and computational domains

Figure 3. Results for stationary cylinders: root-mean square value of lift coefficient (a) and dimensionless vortex shedding frequency (b) compared to published results

Figure 4. Elastically supported cylinder results: root-mean-square value of transverse (a) and streamwise displacement (b) of the cylinder compared to Prasanth and Mittal (2008) and He and Zhang (2016)

Figure 5. Root-mean-square values of transverse cylinder displacement $y_{0rms}$ against Re for $Re_0$=80, 100, 140, 180

Figure 6. Dimensionless transverse vibration frequency for $Re_0$=140, dimensionless vortex-shedding frequency for stationary cylinder $St_0$ (Posdziech and Grundmann, 2007) and reduced natural frequency $F_N$ against Re

Figure 7. Root-mean-square value of transverse cylinder displacement against $U^*St_0$ for $Re_0$=80, 100, 140, 180

Figure 8. Root-mean-square value of lift coefficient against $U^*St_0$ for $Re_0$=80, 100, 140, 180

Figure 9. Root-mean-square value of streamwise cylinder displacement against $U^*St_0$ for $Re_0$=80, 100, 140, 180

Figure 10. Root-mean-square value of drag coefficient against $U^*St_0$ for $Re_0$=80, 100, 140, 180

Figure 11. Root-mean-square value of streamwise cylinder displacement (a) and drag coefficient (b) against $U^*St_0$ (zoom-in) for $Re_0$=100, 140, 180

DOI: https://doi.org/10.1016/j.oceaneng.2018.03.079

DOI: https://doi.org/10.1016/j.oceaneng.2018.03.079

## Table captions

Table 1. Effect of radius ratio $R_2/R_1$ on the cylinder response and force coefficients for Re=150 and $U^*$=5.8837

Table 2. Grid dependence study for Re=150 and $U^*$=5.8837

Table 3. Effect of dimensionless time step $\Delta t$ on the cylinder response and force coefficients for Re=150 and $U^*$=5.8837

Table 4. Dimensionless vortex shedding frequencies for stationary cylinder $St_0$ and the computed constant values $K$ for different Reynolds numbers $Re_0$